CHAPTER 8

CHROMIUM SUBSTITUTED Y-TYPE BARIUM HEXAFERRITE (CO_2-Y); AS A BIOCOMPATIBLE HYPERTHERMIA AGENT

8.1 Introduction

The chromium substituted cobalt-based Y-type barium hexaferrite $Ba_2Co_2Fe_{12-x}Cr_xO_{22}$ (x = 0.0, 0.1, 0.2, 0.3, 0.4 & 0.5) are synthesized using the nitrate-based sol-gel auto combustion method and investigated its potential candidacy as an optional replacement for various soft ferrite materials in the field of magnetic hyperthermia. The proposed hexaferrite samples are prepared using the analytical grades of barium nitrate [$Ba(NO_3)_2$], cobalt nitrate [$Co(NO_3)_3.6H_2O$], ferrous nitrate [$Fe(NO_3)_3.9H_2O$], chromium nitrate [$Cr(NO_3)_3.9H_2O$] as elemental precursors and citric acid [$C_6H_8O_7{\cdot}H_2O$] as a chelating agent or fuel within the process.

To overcome the major issues related to the largely utilized spinel-based ferrite (poor thermo-chemical stability, less heating capability (SAR), less coercivity and magneto-crystalline anisotropy value, poor biocompatibility) and few hexaferrite systems (excess value of coercivity resulting to degrading the heating capability, intermediated anisotropy value), the $Ba_2Co_2Fe_{12}O_{22}$ ferrites are explored with several advantages likewise better thermochemical stability, the highest value of magneto-crystalline anisotropy, coercivity field equivalent to the applied field [(Jotania and Virk, 2012), (Rashid *et al.*, 2013), (Lucht *et al.*, 2019), (Lemine *et al.*, 2020), (Lemine *et al.*, 2014), (He *et al.*, 2018), (Najafinezhad *et al.*, 2018)].

The selection of chromium as a substituting element is inspired by earlier studied ferrite systems, where the replacement of chromium ions at the iron site results in the enrichment of magnetic anisotropy within the soft ferrite systems, such as $Mg_{0.5}Zn_{0.5}Cr_xFe_{2-x}O_4$ [(Haralkar *et al.*, 2012)], $Ni_{0.8}Zn_{0.2}Cr_xFe_{2-x}O_4$ [(Gabal, Al Angari, and Al-Agel, 2015)], $NiCrxFe_{2-x}O_4$ [(Bushkova and Yaremiy, 2018)] as well as in hard ferrite systems such as $BaFe_{12-x}Cr_xO_{19}$ [(Kuznetsov *et al.*, 1999)]. The increase in the anisotropy

energy barrier results in a larger value of specific absorption rate (SAR) or heating capability for the ferrite system [(He *et al.*, 2018)].

The as-prepared nano-crystalline Co_2-Y powders are analyzed using XRD, FTIR, VSM & DLS spectroscopy. After that, these ferrite samples are coated with oleic acid to achieve a well-dispersed ferrofluid. The as-prepared calcined powders are activated using HCl before oleic acid coating. To activate the powder surface, 10 gm of calcined powder is treated by adding 1 M HCl solution within 100 ml of DI water, followed by sonication for 10 minutes. The ferrite powders are retrieved from the solution and washed properly using DI water. After surface activation of ferrite powder, the powder is transferred to another beaker having 100 ml of DI water equipped with vigorous stirring. The pH of the solution is maintained at 9 using the drop-wise addition of ammonium hydroxide solution. After that, 1 wt% of the oleic acid solution is added and allowed for 30 minutes of mixing. Finally, the ferrite particles are obtained in the precipitation form (settled down) after the drop-wise addition of nitric acid (up to the pH value of 5). The precipitate is further washed several times using DI water to remove the unreacted oleic acid. A stable ferrofluid is prepared using the dispersion of 10 mg of oleic acid-coated ferrite powder within 1 ml of DI water, followed by sonication for 5 minutes.

The heating capability of these ferrofluids is governed within the applied AC magnetic field (25 mT at a frequency of 114.1 kHz) in terms of specific absorption rate (SAR) using time-dependent temperature performance. The sample with superior SAR and intrinsic loss power (ILP) performance is further analyzed for its biocompatibility performance with the MG-63 cell line in reference to the control. To evaluate the concentration-dependent cytocompatibility, the samples are dispersed in distilled water with various concentrations, i.e., 2, 5, 10, and 15 mg/ml. The MG-63 cells are procured from the National Center for Cell Science (NCCS) in Pune, India. The cells are grown in

corresponding growth media DMEM (Dulbecco's modified eagle medium), supplemented with 15 % FBS (fetal bovine serum) and 1 % antibiotic in a CO_2 incubator (5 % CO_2 and 95 % relative humidity (RH), Thermofisher Scientific). When the cells are confluent, trypsin-ethylenediaminetetraacetic acid (EDTA), a digestive protease, is added to the cell culture flask to isolate the cells from the surface. The cells present in the prepared suspension are counted using a hemocytometer and equally distributed among 24 wells, with 10^4 cells/ml. The cell-seeded well plate is incubated in a CO_2 incubator to allow cell growth. After 24 hrs of the seeding, different concentrations of sterilized ferrite samples are added to the previously attached cells, and the well plate is further incubated for 24, 48, and 72 hrs for the assessment of particulate cytocompatibility. After a stipulated period, quantitative and qualitative cellular responses are analyzed using MTT (3-(4,5-dimethylthiazol-2-yl)-2,5-diphenyl tetrazolium bromide) assay and fluorescence imaging, respectively. For the MTT assay, after 24, 48, and 72 hrs, the culture media from each well are replaced with the reconstituted MTT (MTT: PBS:: 1:10), and the samples are further incubated for 6 hrs for the formation of formazan crystals by the reaction of MTT and live cells. Thereafter, DMSO (dimethyl sulfoxide) is added to the samples to dissolve the formazan crystals. Now, the absorbance of the obtained solution is measured using an ELISA microplate reader at a wavelength of 595 nm, which indicates the viability of live cells. For the morphological observation of the cells, adhered on the particulate treated wells are fixed with paraformaldehyde (4 %). After that, the fixed cells are permeabilized using triton X (0.1 %), followed by blocking the cells using 1 % bovine serum albumin. The nuclei and cytoskeletons of the blocked cells are stained using Hoechst (Invitrogen) and Alexa FlourPhalloidin (Invitrogen) dye, respectively. The images of the stained cells (nuclei and cytoskeleton) are observed using a fluorescence microscope (LV100 ND, Nikon).

8.2 Results and discussion

The XRD diffractograms of the calcined chromium-substituted barium hexaferrite (Co_2-Y) are shown in Fig. 8.1. The obtained XRD peaks are in good agreement with the standard JCPDS file (card no 440206), which confirms the presence of single-phase Y-type barium hexaferrite ($Ba_2Co_2Fe_{12}O_{22}$) within all samples. The mean crystallite size, lattice constants along with axial (*c/a*) ratio, unit cell volume, X-ray density, and lattice strain are calculated and tabulated in Table 8.1.

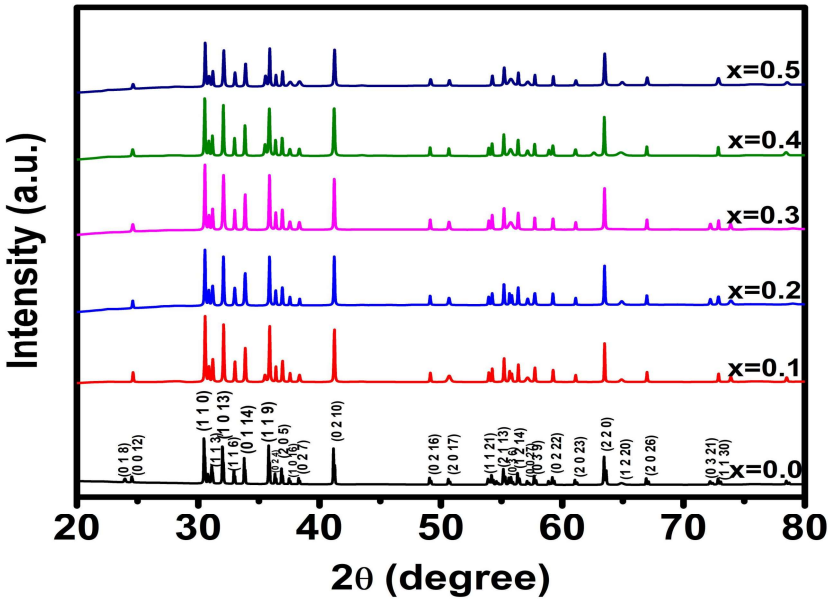

Figure 8.1 XRD patterns of calcined $Ba_2Co_2Fe_{12-x}Cr_xO_{22}$ ($0.0 \leq x \leq 0.5$) hexaferrite samples.

The formation of a single-phase within all the substituted samples confirms the successful substitution of Cr^{3+} ions at the Fe^{3+} site. The substitution decreases the crystallite size along with lattice parameters and unit cell volume. It can be correlated to the replacement of a larger cation (Fe^{3+} = 0.67 Å) with a smaller cation (Cr^{3+} = 0.64 Å) [(Haralkar *et al.*, 2012)]. The axial ratios are found to be varied between 7.423 to 7.426,

which lie within the permissible limit for Y-type barium hexaferrite [(Chandel *et al.*, 2020)].

Table 8.1 The crystallite size, lattice constants (*a* & *c*), axial ratio, unit cell volume, X-ray density, and lattice strain of the calcined $Ba_2Co_2Fe_{12-x}Cr_xO_{22}$ ($0.0 \leq x \leq 0.5$) hexaferrites.

Composition	Crystallite size (nm)	Lattice constants		Axial ratio	Unit cell volume	X-ray density	Lattice strain
		a (Å)	*c* (Å)	(*c*/*a*)	(Å^3)	(g/cm^3)	(ε)
x = 0.0	93.647	5.862	43.525	7.425	1295.201	5.441	-1.32 x 10^{-4}
x = 0.1	74.737	5.850	43.424	7.423	1286.996	5.474	-4.84 x 10^{-4}
x = 0.2	73.420	5.847	43.417	7.425	1285.425	5.478	-9.73 x 10^{-4}
x = 0.3	71.256	5.847	43.407	7.424	1285.423	5.479	-1.03 x 10^{-3}
x = 0.4	71.252	5.844	43.400	7.426	1283.815	5.483	-1.90 x 10^{-3}
x = 0.5	69.595	5.843	43.376	7.424	1282.354	5.488	-2.88 x 10^{-3}

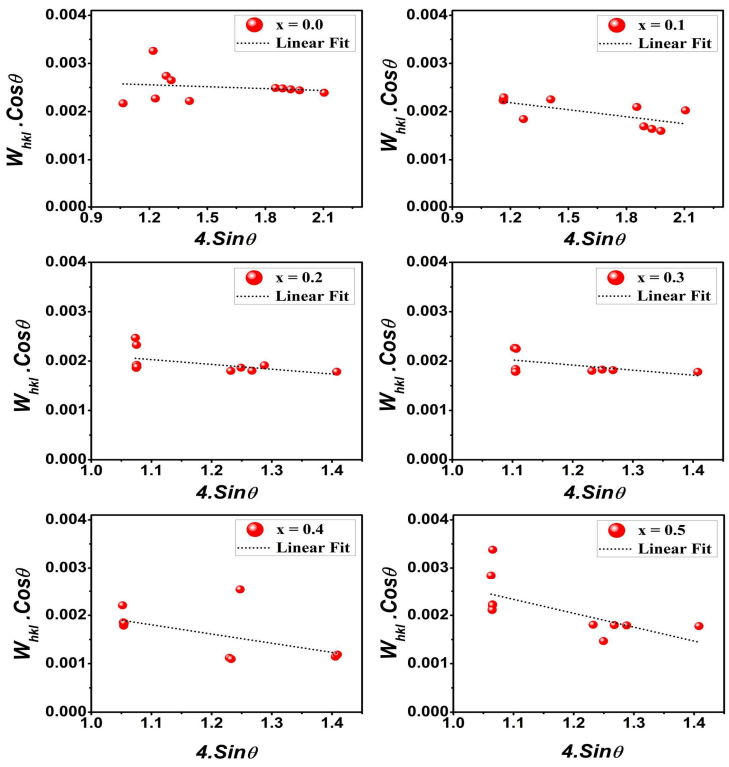

Figure 8.2 Williamson–Hall plot for calcined $Ba_2Co_2Fe_{12-x}Cr_xO_{22}$ ($0.0 \leq x \leq 0.5$) hexaferrite samples.

The X-ray densities are found to be increased with increasing substitution. This increasing trend can be justified due to the dominance of the volumetric contraction of the unit cell over the decreasing molecular weights. The lattice strain is determined using the Williamson-Hall, where the strain (ε) is obtained from the slope of the linear fit to the curve between $W_{hkl}.Cos\theta$ (at y-axis) and $4.Sin\theta$ (at x-axis), as shown in Fig. 8.2. The negative strain depicts the unit cell contraction, which keeps growing continuously with increasing chromium ions substitution.

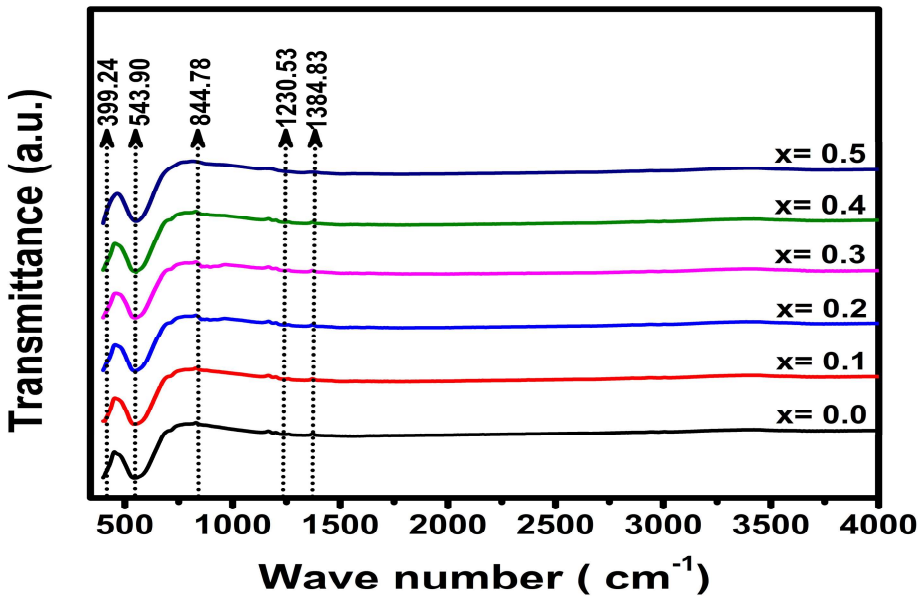

Figure 8.3 FT-IR spectra of calcined $Ba_2Co_2Fe_{12-x}Cr_xO_{22}$ ($0.0 \leq x \leq 0.5$) hexaferrite samples.

The FTIR is employed to estimate the chemical bonding and structural variations within the powdered sample by absorbing a particular wavelength from a band of wavelength. The absorption of a specific wavelength alters the vibrational mode of bonds present within the sample. The presence of a particular structural bond is determined by corresponding to that absorbed wavelength. The FTIR spectrum of chromium substituted Y-type barium hexaferrite (Co_2-Y) is shown in Fig. 8.3.

The presence of two foremost bands near 399 cm^{-1} and 543 cm^{-1} confirms the presence of characteristics intrinsic metal cation vibrations (asymmetric stretching) positioned at octahedral and tetrahedral spaces, respectively. Especially in the case of Y-type hexagonal ferrite, these characteristic peaks may be associated with the cationic vibrations within the spinel block [(Suthar *et al.*, 2020)]. The result shows that these characteristic bands slightly shift towards the higher wavenumber with an increasing chromium concentration because the Cr^{3+} ions are lighter than Fe^{3+} ions. The force-constant (F) and bond lengths (L_b) of Fe-O are calculated and tabulated in Table 8.2.

Table 8.2 Characteristic wave number, effective mass, force constant, and corresponding bond length for Fe-O bond of the calcined $Ba_2Co_2Fe_{12-x}Cr_xO_{22}$ ($0.0 \leq x \leq 0.5$) hexaferrites.

Composition	Wave number (cm^{-1})	Effective mass (10^{-26} kg)	Force constant, (N/cm)	Bond length (Fe–O) (Å)
x = 0.0	543.9039	2.0648	2.1695	1.9862
x = 0.1	545.8327	2.0648	2.1849	1.9815
x = 0.2	547.7615	2.0648	2.2003	1.9768
x = 0.3	549.6902	2.0648	2.2159	1.9722
x = 0.4	551.6189	2.0648	2.2314	1.9676
x = 0.5	553.5476	2.0648	2.2471	1.9630

The result shows that the Fe-O bond length is minimized by increasing the chromium substitution in the system. These results are in good agreement with the volumetric contraction obtained from the XRD results. The presence of a few minor absorption peaks corresponding to 844 cm^{-1} for the C–N=O bond [(Naseri *et al.*, 2010)], 1230 cm^{-1} for the C–C bond [(Naseri *et al.*, 2010)], and 1384 cm^{-1} for twisting (in stretching mode) of the C-H bond [(Iqbal *et al.*, 2014)] are also observed, respectively.

To investigate the role of chromium substitution on the magnetic properties of Y-type barium hexaferrite (Co_2-Y), room temperature (300 K) hysteresis loops are recorded up to an applied field of ±7 Tesla. The results, shown in Fig. 8.4, confirm the existence of ferrimagnetic nature in all ferrites. As it is found that the sample doesn't achieve saturation within the applied magnetic field range, the exact value of saturation magnetization is estimated at the high-field regime using the Stoner–Wohlfarth law of approach (shown in Fig. 8.5). The values of saturation magnetization (M_s), magnetic retentivity (M_r), coercivity (H_c), Bohr magneton (N_{BM}), squareness ratio (S_R), magnetic anisotropy constant (K_1), and effective magneto-crystalline anisotropy constant (K_{eff}) are calculated and tabulated within Table 8.3.

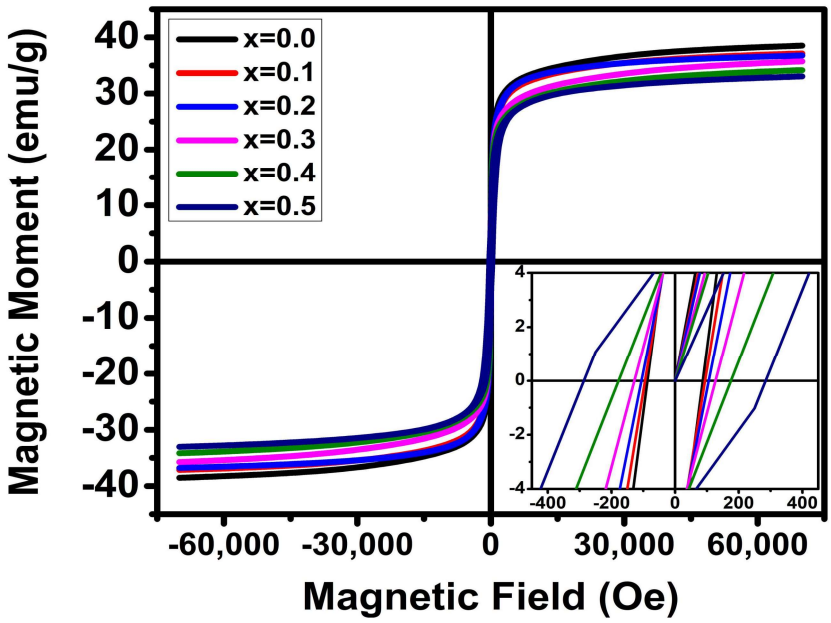

Figure 8.4 Magnetic hysteresis loops (measured at room temperature) of calcined $Ba_2Co_2Fe_{12-x}Cr_xO_{22}$ ($0.0 \leq x \leq 0.5$) hexaferrite samples.

The results suggest that the saturation magnetization (M_s), remanent magnetization (M_r), and Bohr magneton number (N_{BM}) are found to be in decreasing trend with increasing

chromium ion substitution. The decreasing trend for magnetization can be explained due to the replacement of Fe^{3+} ions (larger magnetic moment = $5\mu_B$) with Cr^{3+} ions (less magnetic moment = $3\mu_B$) [(Gabal, Al Angari, and Al-Agel, 2015)]. This decrement in magnetization is also supported by the earlier study on Cr-substituted Z-type hexaferrite, where the addition of chromium transforms a few Fe^{3+} ions into Fe^{2+} ions [(Magham *et al.*, 2017)]. The decrement of M_r with Cr ion may be affected due to a reduction in density [(Nourbakhsh *et al.*, 2011)]. The magnetic retentivity is intensely subjected to chemistry, orientation, and density. The increasing value of coercivity (H_c) may be supported by the decreasing crystallite size (obtained from XRD results), increasing lattice strain, presence of Fe^{2+} ions in the system, and increasing anisotropy constant value [(Magham *et al.*, 2017), (Sharma *et al.*, 2020)].

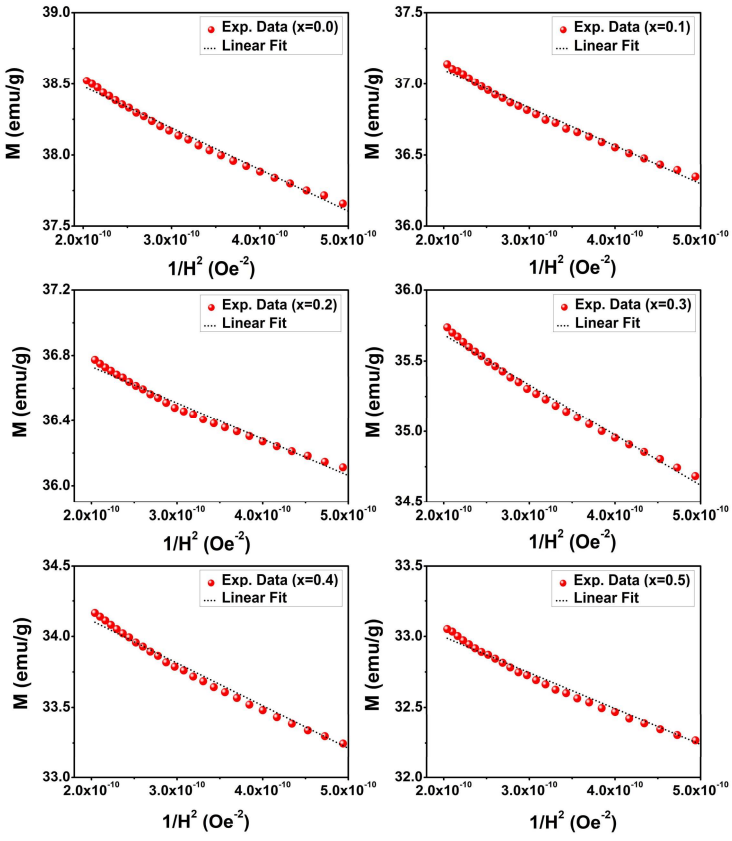

Figure 8.5 M vs. H^{-2} plot (Stoner–Wohlfarth model) of calcined $Ba_2Co_2Fe_{12-x}Cr_xO_{22}$ ($0.0 \leq x \leq 0.5$) hexaferrite samples.

Table 8.3 The saturation magnetization (M_s), magnetic retentivity (M_r), coercivity (H_c), Bohr magneton (N_{BM}), squareness ratio (S_R), magnetic anisotropy constant (K_1), and effective magneto-crystalline anisotropy constant (K_{eff}) of the calcined $Ba_2Co_2Fe_{12-x}Cr_xO_{22}$ ($0.0 \leq x \leq 0.5$) hexaferrite samples.

Composition	M_s (emu/g)	M_r (emu/g)	H_c (Oe)	Bohr magneton (N_{BM})	S_R (M_r/M_s)	K_1 (HA^2/Kg)	K_{eff} (erg/g)
x = 0.0	39.06	7.86	86.87	9.8959	0.2011	1.70×10^{-1}	4.09×10^{6}
x = 0.1	37.63	6.83	94.66	9.5301	0.1814	1.78×10^{-1}	3.77×10^{6}
x = 0.2	37.17	6.31	105.84	9.4119	0.1697	1.97×10^{-1}	3.40×10^{6}
x = 0.3	36.39	5.72	130.14	9.2115	0.1571	2.37×10^{-1}	4.20×10^{6}
x = 0.4	34.71	5.34	173.14	8.7825	0.1538	3.00×10^{-1}	3.02×10^{6}
x = 0.5	33.50	5.12	281.84	8.4743	0.1528	4.72×10^{-1}	3.26×10^{6}

The squareness ratio (M_r/M_s) is analyzed to determine the type of interactions within the ferrite particles. The results show that the squareness ratio (S_R) is found to be in the range of ($0.05 < S_R < 0.5$), which depicts the presence of magnetostatically coupled particles having pseudo-single domain nature [(Adeela *et al.*, 2016)]. The magnetic anisotropy constants (K_1) are found to be in increasing order with the addition of chromium ions into the system. These results are found to be consistent with earlier reported work with strontium hexaferrite ($SrCr_xFe_{12-x}O_{19}$) [(Praveena *et al.*, 2017)]. The experimental values obtained for effective magneto-crystalline anisotropy (K_{eff}) show deviation from the magnetic anisotropy constant and achieve its maximum value of 4.20×10^6 erg/g for x = 0.3. It may be explained due to the combined consideration of several factors likewise surface or volumetric anisotropy (large polydispersion index), and particle shape anisotropy (enhanced role of uniaxial anisotropy), and stress-induced anisotropy [(Srikala *et al.*, 2010)]. Ideally, the effective magneto-crystalline anisotropy (K_{eff}) is expected to

follow a similar trend with coercivity values. This abnormality may be considered due to the competency between the strain-induced coercivity and dominance of K_{eff} [(Ucar *et al.*, 2014)].

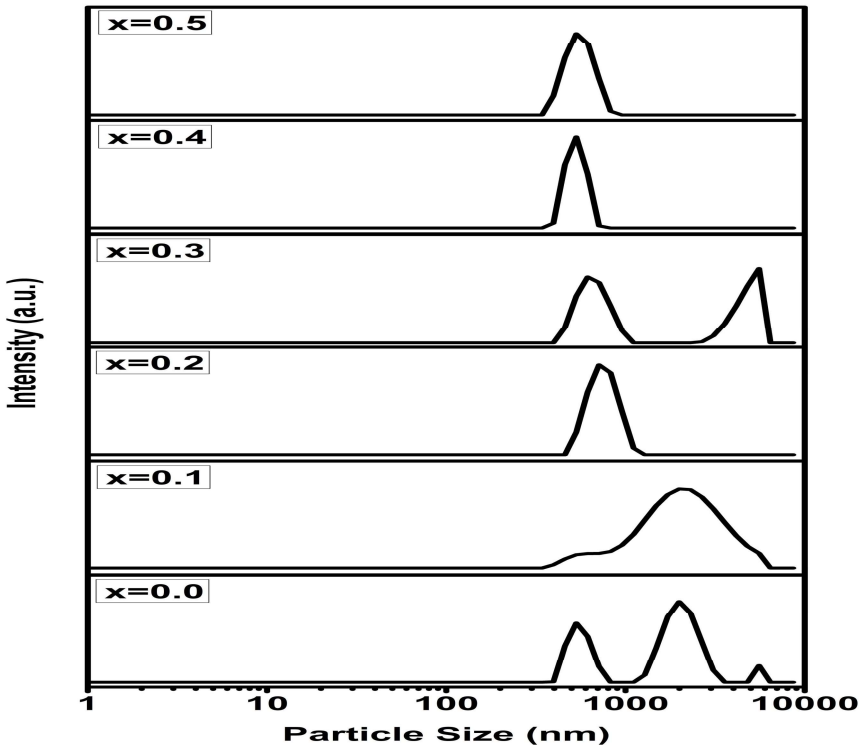

Figure 8.6 DLS analysis for the particle size distribution of oleic acid-coated $Ba_2Co_2Fe_{12-x}Cr_xO_{22}$ ($0.0 \leq x \leq 0.5$) hexaferrite samples.

All the prepared ferrofluids, stabilized using oleic acid and dispersed within DI water, are analyzed for their mean particle size using the dynamic light scattering technique (shown in Fig. 8.6). The obtained mean particle size and poly-dispersion index (PDI) are tabulated in Table 8.4. The particle sizes are shown a decreasing trend (from 2.06 µm to 1.08 µm) with the incorporation of chromium ions into the ferrite system. The PDI value depicts the powder quality with respect to the particle size distribution. Generally, the PDI index measures the degree of non-uniformity within the population-based on particle sizes. The PDI value varies from 0 for dispersion with monosized particles to 1 for a highly poly-

dispersed sample, including multiple particle size populations [(Danaei *et al.*, 2018)]. The PDI value is found to be increased from 0.602 for undoped (x = 0.0) to 0.881 for doped (x = 0.5). The literature suggests that the case of ferrofluids consisting of platelet-shaped ferrite particles having large PDI index values are disadvantageous in terms of the stability of dispersion and SAR values [(Mertelj *et al.*, 2013), (Joshi *et al.*, 2009)].

Table 8.4 The mean particle size, poly-dispersion index (PDI), initial heating rate (dT/dt), specific absorption rate (SAR), and intrinsic loss power (ILP) of oleic acid-coated $Ba_2Co_2Fe_{12-x}Cr_xO_{22}$ ($0.0 \leq x \leq 0.5$) hexaferrite samples.

Composition	Mean particle Size (nm)	Poly-dispersion index (PDI)	Slope (dT/dt)	SAR (W/g)	ILP (nHm^2/Kg)
x = 0.0	2062	0.602	0.0931	38.97	0.86
x = 0.1	1710	0.277	0.1184	49.56	1.09
x = 0.2	1654	0.639	0.1399	58.56	1.29
x = 0.3	1621	0.705	0.2016	84.39	1.86
x = 0.4	1403	0.855	0.1726	72.25	1.59
x = 0.5	1081	0.881	0.1496	62.62	1.38

The oleic acid stabilized $Ba_2Co_2Fe_{12-x}Cr_xO_{22}$ ($0.0 \leq x \leq 0.5$) hexaferrite particles, dispersed within DI water at 10 mg/ml concentration, are investigated for their magnetic hyperthermia capability under an applied field of 25 mT at a frequency of 114.1 kHz. The obtained temperature vs. time graph is shown in Fig. 8.7(a). The dynamic value of temperature is measured using an optical fiber-based probe with better precision (error of ± 0.1°C). The measured quantity (1 ml) of ferrofluid (concentration of 10 mg/ml) is taken into a micro-centrifuge tube and placed inside the magnetic coil arrangement. The SAR values (W/g) and intrinsic power losses (ILP) values under the influence of an externally

applied AC magnetic field are calculated and tabulated within Table 8.4, and the variation of these values along with chromium concentration (x) is shown in Fig. 8.7(b).

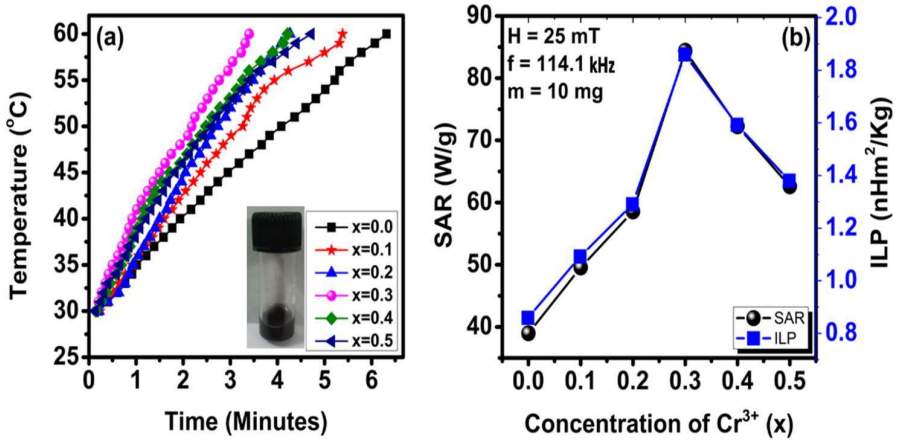

Figure 8.7 (a) The temperature vs. time plots, and (b) variation of SAR and ILP values with chromium concentration for the ferrofluids composed of oleic acid-coated $Ba_2Co_2Fe_{12-x}Cr_xO_{22}$ ($0.0 \leq x \leq 0.5$) hexaferrite samples.

The Fig. 8.7 suggests that the chromium ion concentration initially enhances both SAR (from 38.97 to 84.39 W/g) and ILP (from 0.86 to 1.86 nHm^2/Kg) values up to x = 0.3 compositions and then gradually decreases afterward. The enhancement can be correlated to the increased value of the magnetic anisotropy constant (K_1) as well as the coercivity values below the applied AC magnetic field ($Hc < H_{AC}$). The further enhancement of chromium ions into the hexaferrite system increases the anisotropy-constant value. The decreasing behavior of SAR value within samples (x > 0.3) may be explained by the combined impact of several negative factors such as decreasing particle size, reduced magnetization value, and enhanced value of PDI. Especially for x = 0.5, the coercivity becomes nearly equal to or larger than the applied field of 25 mT (~250 Oe), which hinders the complete reversal of magnetization within the applied field and results in a lower value of both SAR and ILP parameters. The $Ba_2Co_2Fe_{11.7}Cr_{0.3}O_{22}$ composition is found to have

the largest SAR and ILP values with enhanced magnetic anisotropy constant (K_1 = 0.237 HA^2/Kg) and the most significant value of effective magneto-crystalline anisotropy (K_{eff} = 4.20 x 10^6 erg/g) among all the ferrite samples. The received trend for SAR and ILP can be summarized due to the dominance of increasing anisotropy constant up to x = 0.3 composition and the dominance of decreasing particle volume and magnetization value after x = 0.3 composition.

The chromium substituted sample (x = 0.3), which shows the largest value of SAR and ILP, is analyzed through XPS for its elemental valency. The XPS spectra, recorded within the range of 1350 eV to 1 eV for $Ba_2Co_2Fe_{11.7}Cr_{0.3}O_{22}$ ferrite, are shown in Fig. 8.8.

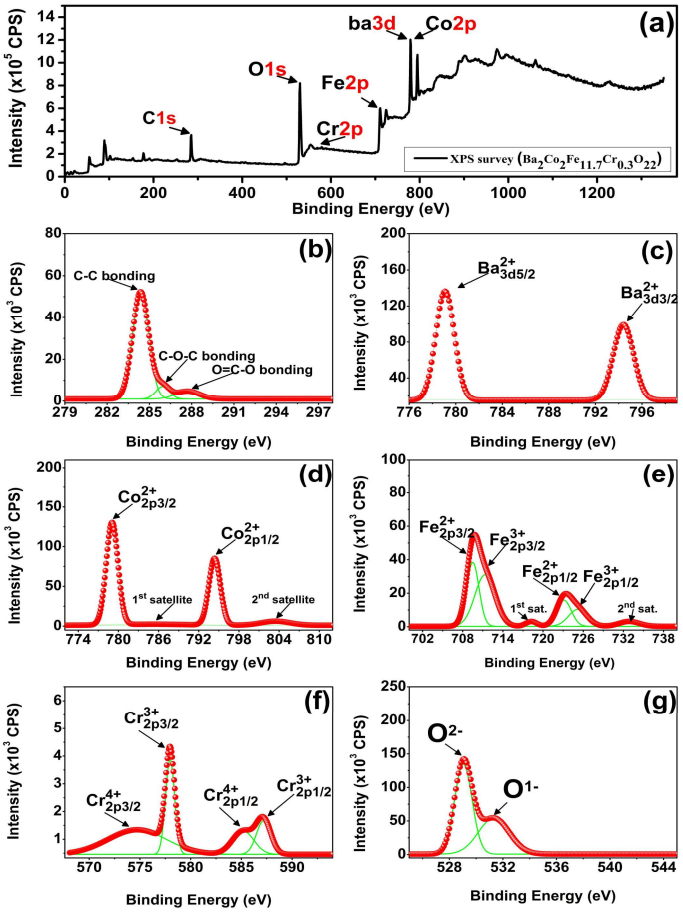

Figure 8.8 The XPS analysis of $Ba_2Co_2Fe_{11.7}Cr_{0.3}O_{22}$ hexaferrite (a) wide scan XPS survey and high-resolution core spectra of (b) C-1*s* (c) Ba-3*d* (d) Co-2*p* (e) Fe-2*p* (f) Cr-2*p*, and (g) O-1*s*.

The XPS survey [Fig. 8.8(a)] confirms the existence of all desired elements, likewise Ba, Co, Cr, Fe, and O, without any other contamination except carbon. The high-resolution C-1*s* peak [Fig. 8.8(b)] is adjusted to 284.8 eV to rectify the binding energy values for all other peaks [(Suthar *et al.*, 2020)]. The deconvolution of C-1*s* spectra confirms the presence of three peaks, corresponding to the 284.8 eV for C-C bonding, 285.93 eV for C-O-C bonding, and 287.71 eV for O=C-O bonding, respectively [(Wu, Lin, and Xu, 2019)]. The high-resolution Ba-3*d* core spectra [Fig. 8.8(c)] approves the existence of two characteristics of spin-orbit doublet for barium, having separation energy of 15.33 eV, corresponding to Ba-3$d_{5/2}$ at 779.08 eV and Ba-3$d_{3/2}$ at 794.41 eV [(Suthar *et al.*, 2020)]. The high-resolution Co-2*p* core spectra [Fig. 8.8(d)], which coexists within Ba-3*d* spectra, confirms the existence of two main characteristics peaks for cobalt, having separation energy of 15.32 eV, corresponding to Co-2$p_{3/2}$ at 779.06 eV and Co-2$p_{1/2}$ at 794.38 eV along with two satellite peaks positioned at 785.09 eV and 803.48 eV, respectively [(Suthar *et al.*, 2020)]. The high-resolution Fe-2*p* core spectra [Fig. 8.8(e)] confirm the presence of two characteristic peaks for iron, having separation energy of 13.61 eV, corresponding to the Fe-2$p_{3/2}$ at 709.79 eV and Fe-2$p_{1/2}$ at 723.40 eV along with two satellite peaks at 718.25 eV and 732.87 eV, respectively. Further, the deconvolution of these two characteristic peaks confirms the coexistence of Fe^{3+} and Fe^{2+} within the sample. These two main peaks are fitted with two spin-orbital doublets for each corresponding to the Fe^{2+}-2$p_{3/2}$ at 709.50 eV, Fe^{2+}-2$p_{1/2}$ at 723.11 eV, Fe^{3+}-2$p_{3/2}$ at 711.33 eV and Fe^{3+}-2$p_{1/2}$ at 725.20 eV, respectively [(Suthar *et al.*, 2020)]. The high-resolution Cr-2*p* core spectra [Fig. 8.8(f)] confirm the existence of two main characteristic peaks for chromium, having an energy separation of 9 eV, corresponding to Cr-2$p_{3/2}$ at 577 and Cr-2$p_{1/2}$ at 586 eV. Further, deconvolution of these two peaks is fitted with two spin-orbital doublets for each peak corresponding to the Cr^{3+}-2$p_{3/2}$ at 57.97 eV, Cr^{4+}-2$p_{3/2}$ at 574.73 eV, Cr^{3+}-2$p_{1/2}$ at

587.20 eV, and Cr^{4+}-$2p_{1/2}$ at 585.17 eV, respectively [(R Aquino *et al.*, 2017)]. The result suggests the coexistence of chromium in both Cr^{3+} and Cr^{4+} oxidation states within the ferrite sample. The high-resolution O-1*s* core spectra [Fig. 8.8(g)] confirms the presence of lattice oxygen (O^{2-}) corresponding to the peak at 529.04 eV and oxygen vacancy associated with the peak position of 531.32 eV. The XPS analysis suggests the presence of mixed elemental oxidation states for both iron and chromium. The presence of Fe^{2+} within the sample clarifies the transformation of Fe^{3+} to Fe^{2+}, which explains the enhanced value of coercivity for chromium substituted samples. The presence of oxygen vacancy (suggested from O-1*s* spectra) may also be considered as an additional factor for the enhancement of SAR value by developing higher conductivity regions (maximizing eddy current losses within applied AC magnetic field) [(Zuo *et al.*, 2022)].

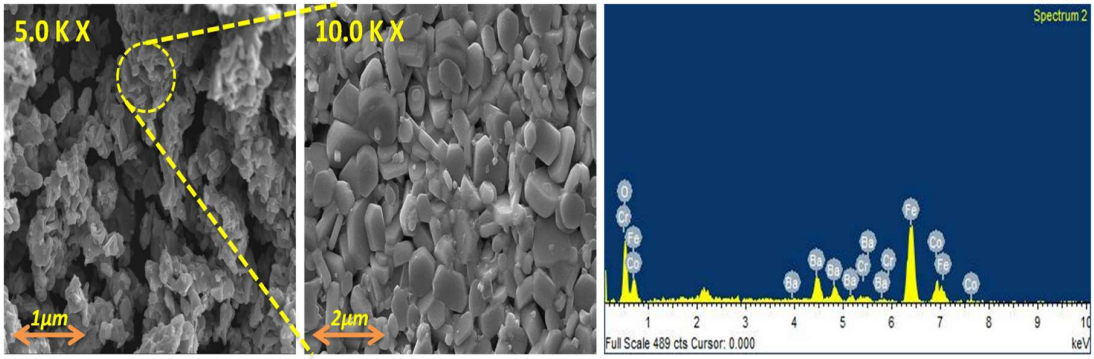

Figure 8.9 SEM micrographs along with EDX spectra of calcined $Ba_2Co_2Fe_{11.7}Cr_{0.3}O_{22}$ hexaferrite powder.

The microstructural features of chromium substituted Y-type barium hexaferrite ($Ba_2Co_2Fe_{11.7}Cr_{0.3}O_{22}$) are analyzed using scanning electron microscopy. Fig. 8.9 shows the micrographs of calcined powder at 5K and 10K magnifications and EDX spectra, which confirms the chemical identity without foreign elements in the system. The surface morphology reveals that the particles have a wide range (from 0.69 to 2.13 µm) of the size distribution (SD = 0.565) and a nearly hexagonal plate-like shape.

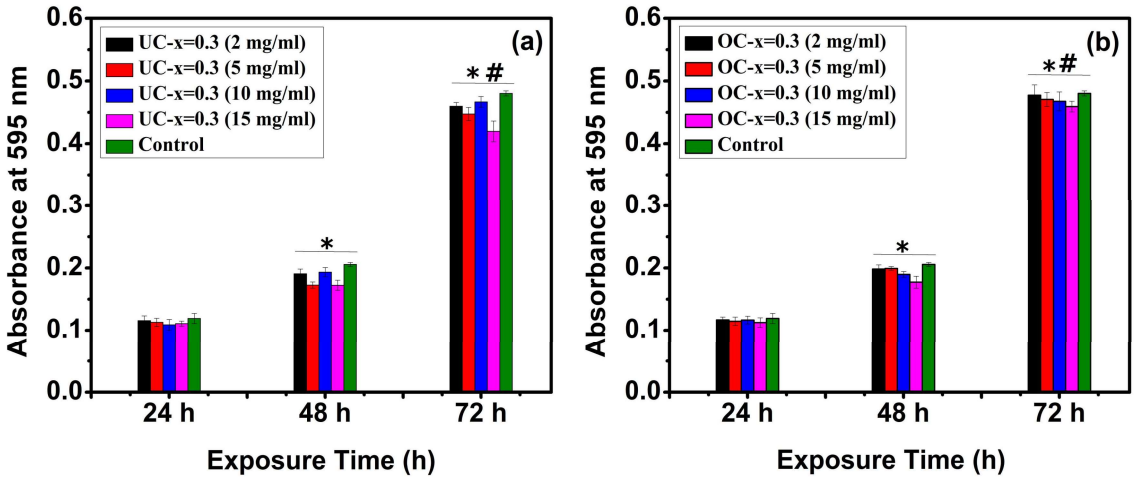

Figure 8.10 Time and concentration-dependent quantitative analysis (MTT assay) for viability response of pristine (UC) and oleic acid-coated (OC) $Ba_2Co_2Fe_{11.7}Cr_{0.3}O_{22}$ hexaferrite powder. The asterisk (*) symbol represents the statistically significant difference at $p \leq 0.05$ in mean optical density (OD) among all of the samples treated for 48 and 72 hrs with respect to the samples treated for 24 hrs. The symbol (#) represents the significant difference at $p \leq 0.05$ in mean OD among all the samples, treated for 72 hrs with respect to the samples, treated for 48 hrs. Error bars: 95 % CI.

The *in-vitro* biocompatibility of uncoated (UC- $Ba_2Co_2Fe_{11.7}Cr_{0.3}O_{22}$) and oleic acid-coated (OC- $Ba_2Co_2Fe_{11.7}Cr_{0.3}O_{22}$) samples are performed using Osteosarcoma MG-63 cells. The MG-63 is categorized as a bone-cancer-based cell line [(Moise *et al.*, 2018)]. The selection of the MG-63 cell line for this study is favored due to its adherent nature, which allows an accurate *in-vivo* simulation (easily adaptable to clinical applications) compared to the suspended cell lines [(He *et al.*, 2018)]. Selected cell lines, upon incubation for 24 hrs, are treated with 4 different concentrations (2, 5, 10, 15 mg/ml) of pristine and oleic acid-coated $Ba_2Co_2Fe_{11.7}Cr_{0.3}O_{22}$ samples for 3 days. The optical absorbance value, which is a direct representation of living cell viability at a wavelength of 595 nm, is measured. The MTT analysis result, as shown in Fig. 8.10, clearly demonstrates the

comparable viability within all prepared ferrite samples in reference to the control (having zero ferrite content). In addition, a significant increase in viability is observed with an increase in the exposure duration for all the treated samples. The viability results clearly suggest that the presence of these ferrite particles doesn't affect the growth of these cells adversely, either mechanically or chemically, i.e., both the pristine and coated $Ba_2Co_2Fe_{11.7}Cr_{0.3}O_{22}$ ferrite are cytocompatible, even up to longer exposure of 72 hrs.

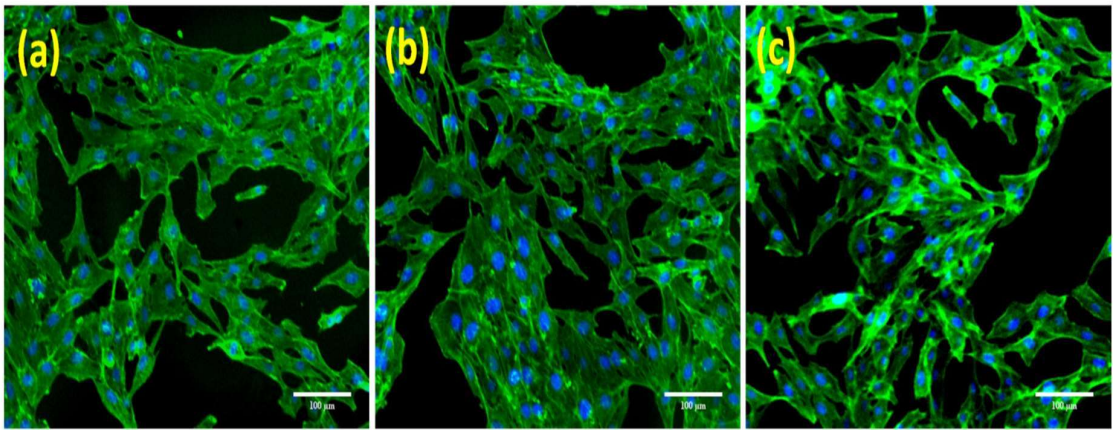

Figure 8.11 Fluorescence microscopy images representing the adherence of MG-63 cells after the exposure of the highest studied concentration, i.e., 15 mg/ml (after 72 hrs), within (a) pristine $Ba_2Co_2Fe_{11.7}Cr_{0.3}O_{22}$ hexaferrite powder, (b) Oleic acid-coated (OC) $Ba_2Co_2Fe_{11.7}Cr_{0.3}O_{22}$ hexaferrite powder, and (c) control.

As shown in Fig. 8.11, the fluorescence images of cell growth suggest the proliferation and enhanced adherence of the cells with both coated and uncoated ferrite particles. A similar trend of cell proliferation was also reported recently with M-type barium hexaferrite within silk proteins [(Xue *et al.*, 2021)]. Interestingly, a minor enhancement in cell viability within oleic acid-coated ferrites particles is noticed. It is in good agreement with the earlier reported studies with oleic acid coatings over the ferrite [(Somvanshi *et al.*, 2020)].

8.3 Summary

The present work proposes the suitability of chromium substituted Y-type barium hexaferrite with enhanced magnetic anisotropy and moderate coercivity value for magnetic hyperthermia applications. The single-phase $Ba_2Co_2Fe_{12-x}Cr_xO_{22}$ ($0.0 \leq x \leq 0.5$) hexaferrite samples are synthesized successfully using the citrate-nitrate auto-combustion method. The room temperature magnetic properties, which play a crucial role in selecting ferrite with high SAR and ILP values, are measured to determine the anisotropy constant and coercivity field. The squareness ratio (S_R) suggests the development of pseudo-single domain nature in all synthesized ferrite samples. The surface of the ferrite particles is functionalized using oleic acid to overcome the issue associated with ferrofluid stability. The oleic acid-coated ferrite is dispersed well within the DI water and studied its magnetic hyperthermia capabilities. The particle size measurement shows that the mean particle size is found to be decreased with the chromium substitution into the system. The magnetic heating performances are analyzed by applying an AC magnetic field of 25 mT at a frequency of 114.1 kHz. The $Ba_2Co_2Fe_{11.7}Cr_{0.3}O_{22}$ composition attains the highest value of SAR, i.e., 84.39 W/g, and ILP value of 1.86 nHm^2/Kg. Finally, both the pristine and oleic acid-coated ferrite particles are analyzed for their biocompatibility using the MG-63 cell line. The result shows that both of these particles are found to favor cell growth and proliferation at all the examined concentrations. The obtained performance of the ferrite materials may be utilized within various biomedical applications such as MRI cell tracking combined with hyperthermia due to its enhanced SAR, ILP, and biocompatibility properties.